JOURNAL OF APPLIED PHYSICS **113**, 054506 (2013)

Diffusion barrier properties of molybdenum back contacts for $Cu(In,Ga)Se_2$ solar cells on stainless steel foils

P. Blösch,[1,a)] F. Pianezzi,[1] A. Chirilă,[1] P. Rossbach,[2] S. Nishiwaki,[1] S. Buecheler,[1] and A. N. Tiwari[1,a)]

[1]*Laboratory for Thin Films and Photovoltaics, Swiss Federal Laboratories for Materials Science and Technology (Empa), Ueberlandstrasse 129, 8600 Duebendorf, Switzerland*

[2]*Nanoscale Materials Science, Swiss Federal Laboratories for Materials Science and Technology (Empa), Ueberlandstrasse 129, 8600 Duebendorf, Switzerland*

(Received 28 July 2012; accepted 11 January 2013; published online 6 February 2013)

Flexible $Cu(In,Ga)Se_2$ (CIGS) solar cells on stainless steel foils face the problem of efficiency deterioration when iron impurities diffuse into the absorber layer. The influence of the magnetron sputtering conditions and the design of Mo-based back contacts on the property of the diffusion barrier against iron is reported here for high efficiency CIGS solar cells grown at low substrate temperatures ($T_{max} = 475\,°C$). The overall material density of the Mo back contact was identified as the dominant parameter for the impurity diffusion barrier performance. It was found that this is also true for Mo bilayer contacts, which show enhanced film densities at low residual stress. The iron diffusion profile in the back contact and CIGS was measured by secondary ion mass spectroscopy, where a linear decrease in the iron impurity concentration in the CIGS towards the CdS buffer layer was found. Furthermore, this iron distribution in CIGS and its consequences on the solar cell efficiency is discussed, supported by defect analysis measurements and photovoltaic device simulations. With a stress-free ~500 nm thick Mo bilayer back contact, best solar cell efficiencies above 15% were achieved with antireflection coating. © *2013 American Institute of Physics*. [http://dx.doi.org/10.1063/1.4789616]

I. INTRODUCTION

The $Cu(In,Ga)Se_2$ chalcopyrite compound (also called CIGS) is an established material for high performance thin film solar cells. On rigid soda-lime glass substrates photovoltaic conversion efficiencies up to 20.3% are reported,[1] which represents the highest thin film solar cell performance on lab-scale. The CIGS technology is also used for flexible substrates such as plastic or metal foils, which can enable low cost production owing to their applicability to roll-to-roll manufacturing systems. Certified efficiencies of 18.7% on polyimide[2] and 17.7% on stainless steel (SS)[3] foils were achieved on lab-scale so far.

In comparison to polyimide substrates, stainless steel foils show higher temperature stability and tensile strength, where CIGS process temperatures up to 600 °C are possible to apply. However, a major disadvantage of steel substrates is that iron as the main component of stainless steel can diffuse through the back contact into the CIGS absorber, where Fe impurities are known to reduce the solar cell performance.[4] To prevent iron diffusion, oxide[5–9] (e.g. Al_2O_3, SiO_2) or nitride[10] (e.g., TiN, Si_3N_4) diffusion barrier layers are conventionally used. These barrier layers are deposited with different techniques, such as magnetron sputtering,[5,6,10] plasma-enhanced chemical vapor deposition,[7] thin film anodization,[8] and atomic layer deposition (ALD).[9] The barrier thickness requirements depend on the material and deposition method. For radio frequency (RF) sputtered Al_2O_3 a thickness of 1–3 μm is proposed by Herz *et al.*,[6] whereas for Al_2O_3 deposited with ALD, Park *et al.*[9] found that the film thickness can be reduced to 100 nm. However, the use of thick barrier layers may increase production costs, whereas the rather expensive and slow ALD method is hard to implement on industrial scale. Beside the diffusion barrier blocking performance and production costs, residual film stress must be considered for thin flexible substrates, as stress can lead to structural deformation (foil bending) and thin film micro-cracking.

In this study, a multistage CIGS process at low substrate temperatures (≤475 °C) is used in order to reduce the requirements of the diffusion barrier,[11] owing to the strong temperature dependence of the diffusion constants.[12] The iron diffusion characteristic through a Mo-based back contact into the absorber layer is investigated. Different back contact designs consisting of Ti/Mo/Mo, Mo/Mo, and single-layer Mo are studied, where the Mo layers were deposited at different conditions. The influence of these designs on the back contact microstructure and residual stress is analyzed, as well as their impact on the property of the impurity diffusion barrier against iron and resulting solar cell performance. In addition, the iron distribution in CIGS and its consequences on the solar cell efficiency are discussed, supported by defect analysis measurements and photovoltaic device simulations.

II. IMPURITY DIFFUSION PROCESS

The microstructure, which can be described by the film thickness, crystal sizes and orientations, grain boundaries, and defect density, has a significant influence on the elemental diffusion properties of a thin polycrystalline layer. We assume

[a)]Authors to whom correspondence should be addressed. Electronic addresses: patrick.bloesch@bloesch.ch and ayodhya.tiwari@empa.ch.

 © 2013 American Institute of Physics

that the impurity diffusion process of iron mainly takes place during the CIGS deposition process, where substrate temperatures up to 475 °C are applied. Two different diffusion processes are considered: Iron diffusion from the steel substrate through the back contact into the CIGS layer and iron impurity diffusion within the CIGS layer.

A. Iron diffusion through the back contact

In this study, the back contacts were deposited by magnetron sputtering technique, which generally results in a polycrystalline layer with columnar microstructure.[13] Owing to the relatively low substrate temperature during the CIGS process particular attention is given to grain boundary diffusion, where diffusion of Fe impurities through a polycrystalline metal layer is mainly expected.[12,14–16] Fisher has proposed a mathematical model[17] for the description of diffusion along grain boundaries (see Fig. 1). There is a strong difference in the diffusion coefficient of the grain boundary D_{gb} compared to the bulk D_b. For most metals, the D_{gb} is 4 to 8 orders of magnitude larger than the D_b, depending on the temperature.[16] This can be explained by the lower diffusion activation energy Q found for grain boundaries ($Q_{gb}/Q_b = 0.4$ to 0.6). The reason for a reduced Q value found in grain boundaries as well as on interfaces and surfaces is the lower density of the interfacial materials in these areas, which benefits the atomic mobility and therefore leads to higher diffusion rates. In addition, the substrate-film interface is illustrated in Fig. 1, where even a larger diffusion constant D_s compared to D_{gb} is expected.[16]

If only grain boundary diffusion is considered, the position y and time t dependent concentration of the diffusing element $C(y,t)$ is proportional to the complementary error function:[12]

$$C(y,t) \propto \mathrm{erfc}\left[\frac{y}{2\sqrt{D_{gb}t}}\right]. \tag{1.1}$$

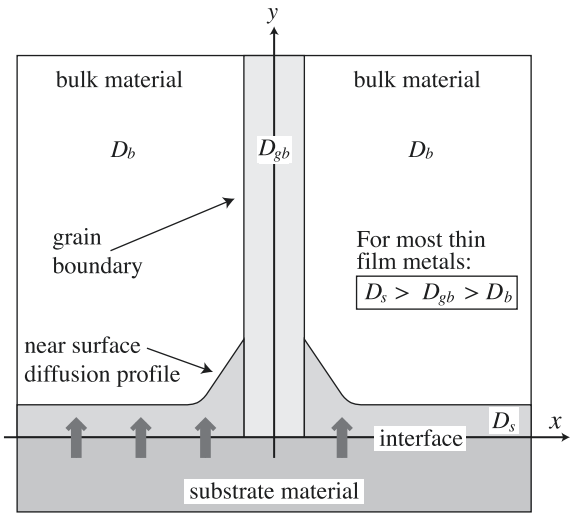

FIG. 1. Schematic shape of the penetration profile of surface, grain boundary, and bulk diffusion (adapted from Heitjans *et al.*[16]). The proposed geometries are from the Fisher model.[17]

B. Iron diffusion within the CIGS layer

When Fe impurities reach the growing absorber layer, they will migrate into the CIGS compound. In this study, a multistage deposition process was used to grow the CIGS layer, which is similar to the process used on polyimide substrates.[2] The CIGS layer is built-up by interdiffusion of the constituent elements during the sequential deposition of In-Ga-Se, Cu-(In-Ga)-Se, and In-Ga-Se. Lundberg *et al.*[18] found that both grain boundary and bulk diffusion are important for this intermixing process, where as an example diffusing atoms move via vacant sites in the crystal. Thus, it can be assumed that for the Fe impurity diffusion process during CIGS growth not only grain boundary but also bulk diffusion must be considered,[19] which will result in a relatively flat diffusion profile throughout the CIGS layer. Tablero *et al.*[20] found from density functional theory calculations of chalcopyrite compounds that Fe can substitute on the cation sites in the CIGS layer. This suggests that Fe can be (at least partly) included into the CIGS compound already during its formation process and therefore follows the interdiffusion paths of the constituent elements.

III. EXPERIMENTAL

The back contact design variation is summarized in Fig. 2, where for each sample (S1–S6) a corresponding reference (RefS1–RefS6) is used for comparison. For the reference designs, a similar layer stack was chosen as reported in a previous study,[10] where solar cell efficiencies up to 17.3% are demonstrated. For each sample-reference pair all process steps after the back contact deposition were done simultaneously. The experimental set includes a design variation (single and bilayer), where two different sputtering conditions (A and B, see Table I for details) were applied, as well as a variation in the overall film thickness (160 and 500 nm). A Ti adhesion layer was used in the reference design because its coefficient of thermal expansion matches to the stainless steel substrate. As a consequence Ti is not affected by thermal stress and is assumed to lower the shear stresses of the whole back contact structure, which improves adhesion.[21]

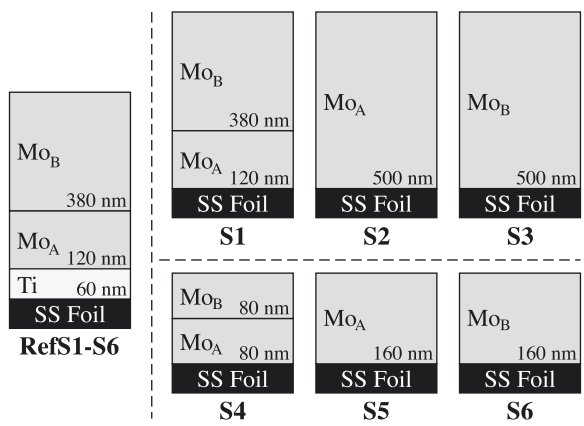

FIG. 2. Different back contact configurations used for the evaluation. The set includes six samples (S1–S6) with corresponding references (RefS1–RefS6). The references additionally have an adhesion-promoting Ti layer.

RIGHTSLINK

TABLE I. Parameters of the Mo sputtering process A and B and the Ti adhesion-promoting layer. The thickness of the layers was controlled by the speed of the substrate movement.

Layer	Power [W/cm^2]	Voltage [V]	RF-Bias [W]	Pressure [Pa]	Dep. Rate [nm/min]
Ti	5.3	430	40	0.28	133
Mo_A	4.0	410	0	0.25	150
Mo_B	2.7	350	0	0.50	105

A. Solar cell process

The 50 μm thick stainless steel foils (ASTM: 430 with 82.6 at% Fe and 16.1 at% Cr) were cleaned in an ultrasonic soap-bath followed by a weak acetic acid and several deionized water baths. The drying was performed with a nitrogen gun. After this cleaning procedure, the samples were mounted onto a substrate holder and transferred to the chamber of a BAS 450 PM magnetron sputtering machine. The stainless steel foils were heated up to 200 °C for one hour in vacuum. After cooling down the foils to room temperature (base pressure $<10^{-7}$ hPa), the samples were plasma cleaned. This treatment was performed for five minutes by an RF substrate bias of 120 W at 1 Pa partial pressure of Ar resulting in about -40 V_{dc} self-biasing of the substrates.

The direct current sputtering process for the back contact layers was performed without external heating of the substrate, where the samples passed the corresponding target for each layer just once (single-pass deposition, target-substrate distance was $\sim$8 cm). After each layer, the direction of the movement was changed. The process parameters are summarized in Table I. For the Ti adhesion-promoting layer, an RF substrate bias of 40 W was applied during the sputtering deposition resulting in a self-biasing of -59 V_{dc}, which provides additional energy to film growth leading to higher film densities.[13]

After the back contact deposition, the $\sim$2.7 μm thick CIGS layer was deposited by a multistage co-evaporation process with maximum substrate temperature of 475 °C. Sodium, which is known to improve the solar cell performance, was incorporated via a NaF post-deposition treatment described by Rudmann *et al.*[22,23] The n-type CdS buffer layer was deposited by a chemical bath deposition method and the ZnO/ZnO:Al front contact by RF magnetron sputtering. To improve the electrical conductivity of the front contact, an additional Ni/Al grid was deposited using masks in an electron-beam evaporation system. A MgF_2 layer was evaporated as antireflection coating (ARC). In the last step, single cells with an area of about 0.3 cm^2 were defined by mechanical scribing.

B. Characterization methods

The back contact layers were characterized by different techniques. The sheet resistance R_{sheet} was measured by four-point probe technique using a SD-600 from Nagy Instruments. The film thickness d was quantified with a profilometer (Ambios XP-1). The electrical resistivity of the films was calculated by multiplying R_{sheet} with d. The surface roughness (S_q) was measured using atomic force microscopy (AFM, nanoSurf), where an area of 2×2 μm^2 in size was analyzed with an uncoated Si tip. The film density was calculated by the weight of the layers measured with a balance (Mettler AT400) divided by the coated area and d. A scanning transmission electron microscope (STEM, JEOL 2200FS) was used for cross-section imaging of the back contact multilayer structure, where an operation voltage of 200 kV was applied. The elemental mapping was performed with the integrated energy-dispersive x-ray spectrometer (EDS) of the STEM microscope. X-ray diffraction (XRD, Siemens D5000) was used to measure the residual stress of the films, where the X-ray radiator was a CuKα1 ($\lambda = 1.54056$ Å) operated at 40 mA and 40 kV. With the "$\sin^2(\Psi)$" technique,[24,25] the residual stress was determined from the Mo $\langle 211 \rangle$ peak.

The completely processed solar cells were electrically characterized by current density to voltage (JV), external quantum efficiency (EQE), and capacitance to voltage (CV) measurement techniques. With the JV method, the diode characteristic of the solar cell was measured under standard conditions using AM1.5 illumination at room temperature. The average value of each photovoltaic parameter was calculated from a total of eighteen cells per sample. The charge carrier density was measured by the CV method with an LCR meter from Agilent (E4980A), where the frequency and temperature was 300 kHz and 123 K, respectively. The impurity diffusion profiles were measured with time-of-flight secondary ion mass spectroscopy (ToF-SIMS, ION-TOF ToF.SIMS5). Bi^+ was used as the primary ion for the analysis on a 100×100 μm^2 area on the sample, where an acceleration voltage of 25 kV at 1 pA was applied. The depth profile was performed with O_2^+ ions at 1 kV and 258 nA, where for each cycle an area of 300×300 μm^2 was sputtered for two seconds. The signal intensity of the investigated elements was normalized by the ^{65}Cu intensity, which is assumed to be equal for all samples. The normalized Fe signal of the S4–S6 samples was integrated over the CIGS layer excluding interface regions and divided by the RefS6 reference value in order to calculate the relative Fe concentration in the absorber.

In order to simplify the density, resistivity, AFM and STEM analysis, similar samples were grown on glass substrates under identical deposition conditions as on the stainless steel foils. The ToF-SIMS and XRD stress measurements, as well as the photovoltaic characterizations of the solar cells, were performed on the stainless steel substrates.

IV. RESULTS AND DISCUSSION

A. Back contact investigation

The Mo back contact properties can be tuned by the sputtering parameters[26–28] as well as by the multilayer design.[29] In this study, two different Mo sputtering processes, A (Mo_A) and B (Mo_B), were investigated (see Table I). It was found that the density increases with the Mo film thickness and that the Mo_A films have higher density compared to Mo_B (see Fig. 3). Thus, the grain boundaries of Mo_A films are more compact with fewer voids in-between. The higher film porosity for process B can be explained by the energy loss of the

RIGHTSLINK

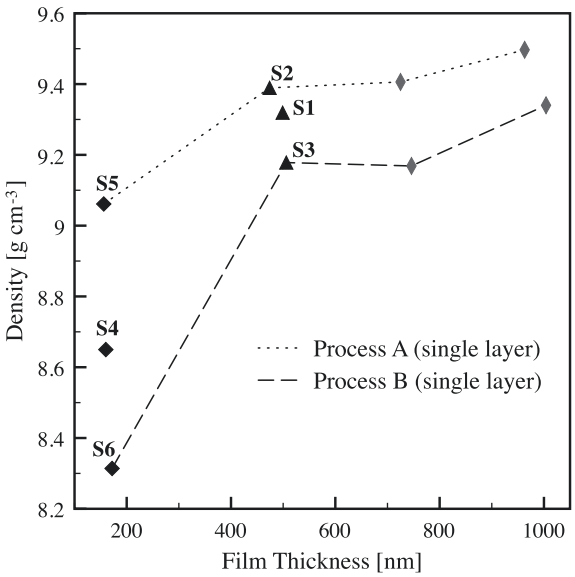

FIG. 3. Density of Mo back contacts versus their thickness and the influence of different deposition conditions (see Fig. 2). The density increases with the film thickness. Films with process A show higher density than with process B. The bulk density of Mo is 10.22 g/cm^3 (at 20 °C).[31]

sputtered Mo particles impinging the substrate. There are two mechanisms for the particle energy loss: (1) Particles leaving the target have a lower initial energy due to the reduced kinetic energy of Ar^+ ions impinging the target (lower acceleration voltage, see Table I). (2) The probability that the sputtered particles undergo collisions with Ar atoms when travelling to the substrate is higher due to the higher partial pressure for process B. Calculations with the simulation program SRIM[30] show that the second mechanism is dominant for the energy loss of the sputtered Mo particles. For processes A and B, sputtered Mo particles have an initial energy of 32.1 eV and 30.5 eV when leaving the target, and 24.6 eV and 17.2 eV when they reach the substrate, respectively. Therefore, the energy available for growing the Mo_B layer is ~30% lower compared to Mo_A.

The samples S1 and S4 in Fig. 3—representing the bilayer designs from Fig. 2—show a density value between those of the Mo_A and Mo_B film series. For S1, the density is slightly higher than expected from the layer thickness ratio of Mo_A and Mo_B, indicating that the thin Mo_A layer has an influence on the microstructure of the second layer leading to a densification of the Mo_B film. Another indication for an adaption of the Mo_B to the Mo_A layer is given by the roughness measurement performed by AFM: Samples S1 and S2 show both an average roughness of $S_q = 4.0 \pm 0.4$ nm, whereas S3 has a ~25% higher roughness of $S_q = 5.1 \pm 0.1$ nm.

The film resistivity decreased with an increasing film density (results not shown), which is in agreement with results from a study by Klabunde *et al.*[32] For the sputtering process conditions Mo_A and Mo_B, a resistivity of $12.7 \pm 0.4\ \mu\Omega$cm (S2) and $15.3 \pm 0.5\ \mu\Omega$cm (S3) was measured, respectively. However, the film resistivity does not play an important role for the solar cell design, because the stainless steel substrate itself provides the main part of the electrical conductivity of the back contact.

Results from the residual stress measurements of samples S1–S6 are shown in Fig. 4. A higher compressive stress was found for S2 and S5 (process A) compared to S3 and S6 (process B). This trend is in good agreement with a previous study.[33] The bilayer samples S1 and S4 show a residual stress value comparable to the samples with process B. This is unexpected because the bilayer designs have a significantly higher density than single layer Mo_B (see Fig. 3). Therefore, we believe that the internal interface of the double-layer back contact designs is responsible for the relaxation in residual stress. The finding of Fig. 3 that with increasing layer thickness the film density also increases conflicts with observations from Klabunde *et al.*,[32] which found no influence of the film thickness on the density. However, this increase in density can be explained by the different sputtering setup used for the experiments: Klabunde deposited the substrates stationary whereas in this work moving substrates were used resulting in a curved shape of the columnar microstructure of the film. With increasing thickness, the diameter of this curve also increases, and therefore the microstructure gets denser. In Fig. 5, the shape of the columnar microstructure of the RefS design is visualized by STEM. The cross-section image shows an abrupt interface between the Ti and Mo_A layers, whereas the grains of Mo_B grow continuously on the grains from the Mo_A layer. Consequently, the grain boundaries of Mo_A and Mo_B are directly interconnected and thus also the Fe diffusion channels. This observation supports the interpretation, that the dense Mo_A bottom layer influences the growth properties of the following Mo_B layer, which leads to high film density of the bilayer stack (see Fig. 3). Furthermore, the EDS profile in Fig. 5 shows a decrease in the Mo signal at the Mo_A/Mo_B interface, which could be explained by a lower density owing to nanovoids located at this interface. This is beneficial to compensate residual film stress, because the porosity at the interface may reduce the overall stress in the contact stack, as observed by XRD measurements shown in Fig. 4.

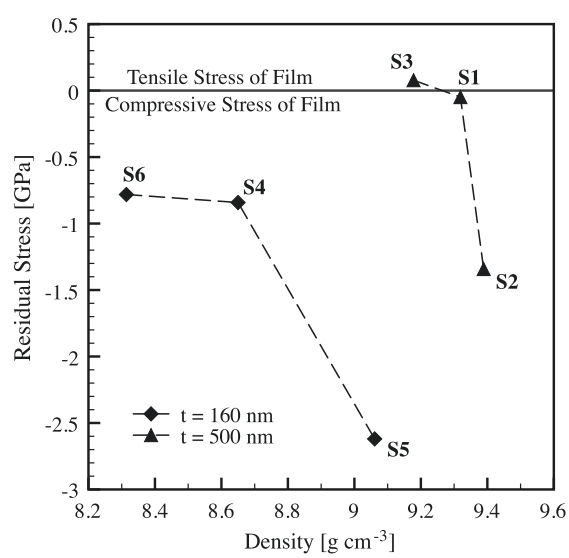

FIG. 4. Residual stress in the back contact films of samples S1–S6. The bilayer designs (S1 and S4) show comparable stress values as single layer Mo_B (S3 and S6), which could be a result of stress relaxation at the interface.

RIGHTSLINK

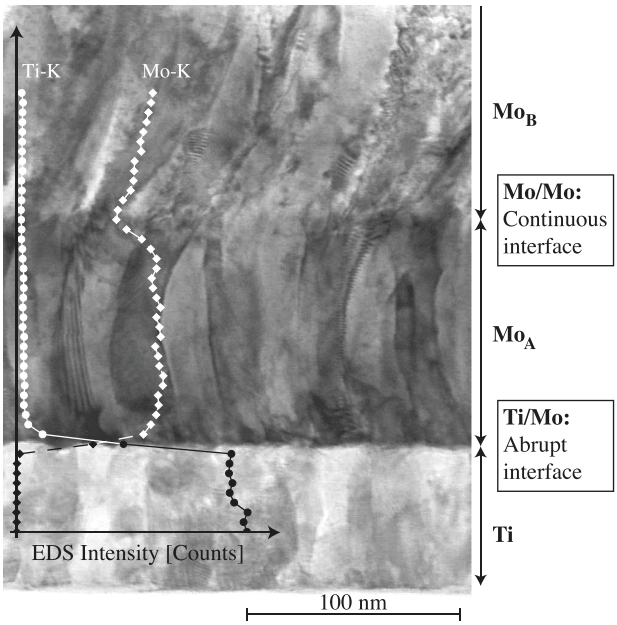

FIG. 5. STEM image of reference contact (RefS) reproduced on glass substrate. The microstructure of the Ti/Mo_A interface shows an abrupt change, whereas the Mo_A/Mo_B interface shows continuous growths of the columns. STEM-EDS mapping profile indicates a lower Mo density at the interface of Mo_A/Mo_B.

B. Impurity diffusion and solar cell results

The Fe impurity concentration in the samples S4, S5, S6, and RefS6 was measured using ToF-SIMS depth profiles. This sample selection was motivated by the observed loss in solar cell efficiency, which will be discussed later. The amount of Fe in CIGS could only be characterized qualitatively because no standard CIGS sample with known Fe concentration was available for SIMS calibration. The Fe concentration for sample S4, S5, and S6 is 7.9, 7.2, and 14.4 times higher compared to RefS6, respectively. For RefS6, the Fe amount in CIGS is equal to that measured on a Fe-free substrate and therefore represents the noise of the ToF-SIMS detector.

For the sample RefS6 (Fig. 6, I), the Fe concentration in the Ti layer shows a constant value of ~1.2 at. %, which was calculated from a Ti calibration probe. For sample S4 (Fig. 6, II), where no Ti adhesion-promoting layer was used, the Fe signal strongly decreases within the Mo_A layer to the impurity level of the used sputtering target material, which is approximately 20 ppm. These observations show that Fe diffusion through the Mo_A layer follows the expected profile for grain-boundary diffusion described by Eq. (1.1). For the Ti layer, a reduction in the Fe signal intensity is only observed at the interfaces and not within the adhesion-promoting layer. At the discrete Ti/Mo_A interface, the boundaries of the columnar grains are not directly interconnected (see Fig. 5), which leads to an interruption of the Fe diffusion channel and therefore to an efficient Fe blocking behavior at this location (see Fig. 6, I). The Fe distribution profiles in the CIGS layer for sample S5 and S6 are shown in Fig. 7. For both profiles, a linear decrease in the Fe impurity concentration within the CIGS layer towards the front is apparent.

JV characteristics are shown in Table II, summarized by the difference of the average efficiency (Eff), fill-factor (FF),

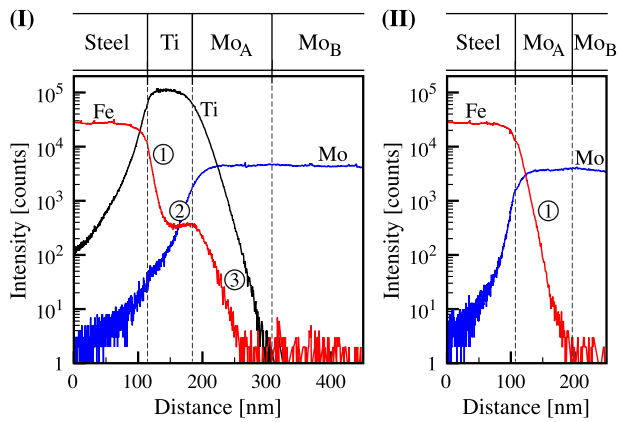

FIG. 6. ToF-SIMS depth profiles of back contact RefS6 (I) and S4 (II) after CIGS processing, showing Fe diffusion towards the CIGS layer. For RefS6, Fe is blocked at the Steel/Ti (1) and Ti/Mo_A interface (3). Inside of the Ti layer (2), the Fe concentration has a constant value of ~1.2 at. %. In case of the sample S4, the Fe concentration strongly decreases starting at the Steel/Mo_A interface (1) and is reduced in the Mo film. The SIMS profiles were sputtered from the front towards the substrate (right to left). To improve visualization, the *x*-axis was scaled with respect to the layer thickness.

open circuit voltage (V_{oc}), and short-circuit current density (J_{sc}) of the samples S1–S6 to their corresponding references RefS1–RefS6. No significant difference in performance was measured for samples with 500 nm thick Mo back contacts (S1–S3), whereas for samples with 160 nm thin contacts (S4–S6), a reduction of all parameters is observed. The highest loss in efficiency of 3.6% (absolute) is observed for S6, which also shows the lowest film density of all samples investigated. A strong correlation between the back contact density, Fe concentration in CIGS, and loss in efficiency of the solar cell is apparent from Fig. 8. With increasing Mo film density, a lower Fe concentration is detected in the CIGS layer and higher solar cell efficiency is found. Furthermore, the multilayer back contact design (S4) shows almost the same barrier performance as the high-density sample (S5), even though the density of the back contact is significantly lower. However, the internal interface

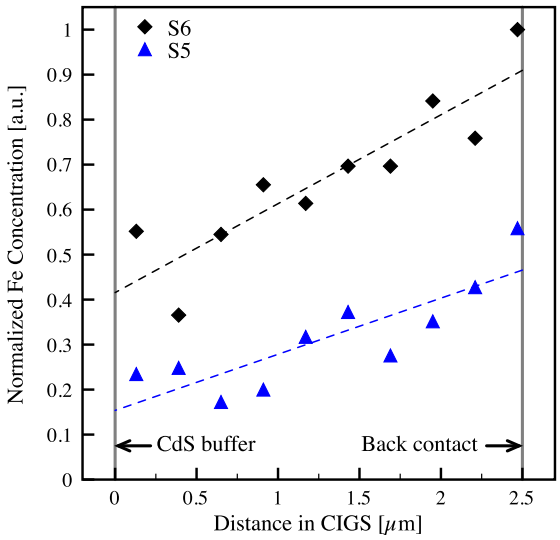

FIG. 7. Normalized Fe distribution profile in CIGS for samples S6 and S5 measured by ToF-SIMS. For both samples, the Fe concentration linearly decreases from the back contact to the CdS buffer layer.

RIGHTSLINK

TABLE II. Summary of JV results, where the average value for each sample (av.) and the difference to the corresponding reference ($\Delta = SX - RefSX$, $X = 1\ldots6$) is shown. An ARC was applied for all cells.

	Eff [%]		FF [%]		V_{oc} [mV]		J_{sc} [mA/cm^2]	
Sample Name	av.	Δ	av.	Δ	av.	Δ	av.	Δ
S1	14.9	0.0	72.5	0.2	658	−1	31.3	−0.1
S2	15.2	−0.1	72.9	1.5	651	−19	32.1	0.1
S3	14.8	0.3	72.7	1.0	647	−5	31.4	0.5
S4	13.8	−1.6	70.6	−1.8	626	−41	31.2	−0.8
S5	13.9	−1.1	71.7	−0.5	631	−17	30.6	−1.3
S6	12.1	−3.6	68.1	−4.5	628	−52	28.4	−3.4

of the double-layer back contact (S4) itself may not provide the enhancement in the diffusion barrier property against Fe, owing to the interconnected grain boundaries and increased porosity at the Mo_A/Mo_B interface (see Fig. 5). It is rather expected that the density of the two individual layers define the diffusion barrier strength against Fe. These layer densities are not sufficiently described by the average film density of the multilayer back contact stack (see Fig. 3), because this measurement also includes the porous area at the internal interface. This interpretation is supported by the strong increase in back contact density from sample S3 to S1 (see Fig. 3), which would not be expected from the layer design (see Fig. 2) and suggests that the Mo_B layer density increased significantly in comparison to S3. In this respect, the influence of the Mo_A microstructure on the grain growth of the Mo_B layer (see Fig. 5), which can result in a significant improvement in film density, might lead to the good diffusion barrier performance of the Mo bilayer back contact sample (S4).

C. Defect analysis and device simulations

The results from Fig. 8 show a strong correlation between the efficiency loss and amount of Fe in the CIGS layer. These findings are in good agreement with measurements from Eisenbarth *et al.*,[34] who found a logarithmic trend for the Fe concentration in CIGS versus the efficiency loss. The photovoltaic efficiency loss originating from Fe defects in the CIGS layer was further analyzed for sample S6 and compared to its reference RefS6. This sample choice was motivated by the strong efficiency decrease observed for sample S6.

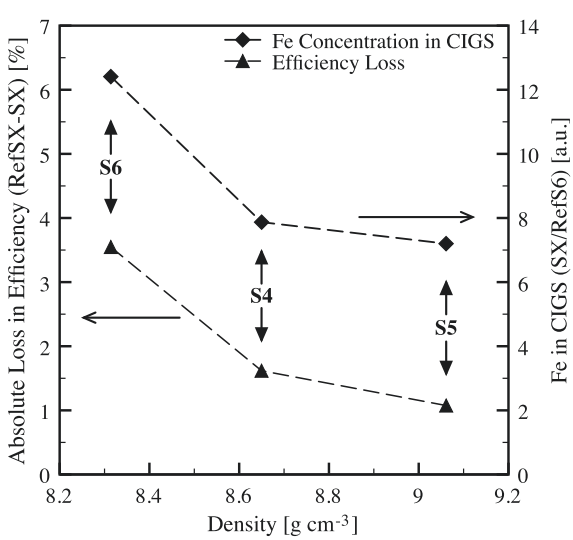

FIG. 8. Influence of the back contact density on the Fe amount in CIGS and loss in cell efficiency compared to the respective reference samples ($X = 4\ldots6$). Increasing the Mo back contact density reduces the Fe diffusion and the loss in efficiency, whereby the bilayer back contact (S4) shows almost the same performance as the high-density Mo_A single-layer sample (S5).

In this work, two different sites in the CIGS lattice were considered to be occupied with Fe impurities, which are Fe on Cu (Fe_{Cu}) and on In/Ga site ($Fe_{In,Ga}$). In case of Fe_{Cu}, a reduction in the density of Cu vacancies can occur when iron occupies free Cu sites, which is the main p-type dopant in the CIGS absorber.[35] For In/Ga site occupation, $Fe_{In,Ga}$ acts as a deep-level defect.[3,34,36,37] The energy level of this deep acceptor defect was observed at 320 meV in polycrystalline CIGS with admittance spectroscopy[3] and in CIS single crystals at 400 meV with optical absorption spectroscopy.[37] As a consequence, $Fe_{In,Ga}$ defects in CIGS will lead to enhanced carrier recombination and thus to a reduction in solar cell performance. We considered two different regions in CIGS where recombination takes place, which is the space-charge (SCR) and quasi-neutral region (QNR). The Fe distribution profile within the CIGS layer (see Fig. 7) shows that the Fe impurity concentration is higher in the QNR than in the SCR, which extends ~400 nm into the CIGS layer. Thus, higher carrier recombination is expected in the QNR part of the CIGS absorber.

In order to discuss the impact of Fe impurity distribution in CIGS on the solar cell performance in detail, SCAPS[38] device simulations were performed. A summary of the main simulation parameters is provided in Table III, whereas most parameters were taken from Gloeckler *et al.*[39] The linearly decreasing behavior of the $Fe_{In,Ga}$ defect concentration (N_{Fe}) from Fig. 7 was implemented into the simulation ($CIGS^L$, see Table III). Additionally, a constant value for the N_{Fe} was used for comparison ($CIGS^C$). An Fe defect energy level of 320 meV was chosen for the simulations, owing to the similar CIGS process used in the corresponding reference.[3] However, the outcome of the simulation with a defect energy level of ~400 meV (as reported by others[34,37]) leads to comparable results.

The acceptor density N_A of S6 was determined from CV measurements (see Fig. 9, I), which is ~3.5 times lower compared to RefS6. As already discussed before, the reduction of N_A, which can be interpreted as a loss in p-type doping of the CIGS absorber, could be explained by Fe_{Cu} defects present in the CIGS layer. For SCAPS simulations, this observation was taken into account by varying the acceptor density N_A opposite to the defect density N_{Fe} (see Table III).

In Figs. 9, II and 9, III, results from JV and EQE measurements and the corresponding SCAPS simulations (with linear gradient and constant N_{Fe}) of S6 and RefS6 are shown. The simulated data of $CIGS^L$ fit to the measurement results, whereas the constant N_{Fe} assumption ($CIGS^C$) leads to an underestimation of the V_{oc}. This can be explained by the higher defect concentration in the SCR for $CIGS^C$ compared to $CIGS^L$. Rau *et al.*[40] describe the influence of recombination on the V_{oc} in both the QNR and SCR, where a stronger

RIGHTSLINK

TABLE III. Summary of the parameters used for SCAPS simulation for samples RefS6 and S6, which are layer width (W), material (ε) and vacuum permittivity (ε_0), bandgap (E_g), electron (μ_e) and hole mobility (μ_h), shallow donor (N_D) and acceptor (N_A) concentration, and effective states in conduction (N_C) and valance (N_V) band. The bandgap of the CIGS layers is graded and was taken from ToF-SIMS measurements (not shown). Additionally, mid-gap state defects were assumed for all layers (N_{mgd}), which are acceptor states for CdS and donor states for the other layers. For sample S6, a $Fe_{In,Ga}$ defect concentration (N_{Fe}) with energy of 320 meV above the valence band was used for the simulation, which was linearly graded for $CIGS^L$ and constant for $CIGS^C$. The RefS6 sample ($CIGS^{Ref}$) was assumed to be Fe-defect free.

Layers:	AZO	ZnO	CdS	$CIGS^{Ref}$	$CIGS^L$	$CIGS^C$
W [nm]	150	80	50	2700	2700	2700
$\varepsilon/\varepsilon_0$	9	9	10	13.6	13.6	13.6
E_g [eV]	3.4	3.4	2.4	Graded	Graded	Graded
μ_e [cm^2/Vs]	100	100	100	100	100	100
μ_h [cm^2/Vs]	25	25	25	25	25	25
N_D [cm^{-3}]	1×10^{18}	5×10^{17}	1.1×10^{18}	-	-	-
N_A [cm^{-3}]	-	-	-	1×10^{16}	$9 \times -2 \times 10^{15}$	5×10^{15}
N_C [cm^{-3}]	2×10^{18}	2×10^{18}	2×10^{18}	2×10^{18}	2×10^{18}	2×10^{18}
N_V [cm^{-3}]	2×10^{19}	2×10^{19}	2×10^{19}	2×10^{19}	2×10^{19}	2×10^{19}
			Defects			
N_{mgd} [cm^{-3}]	1×10^{17}	1×10^{17}	1×10^{18}	1×10^{15}	1×10^{15}	1×10^{15}
N_{Fe} [cm^{-3}]	-	-	-	0	$1 \times -8 \times 10^{15}$	5×10^{15}

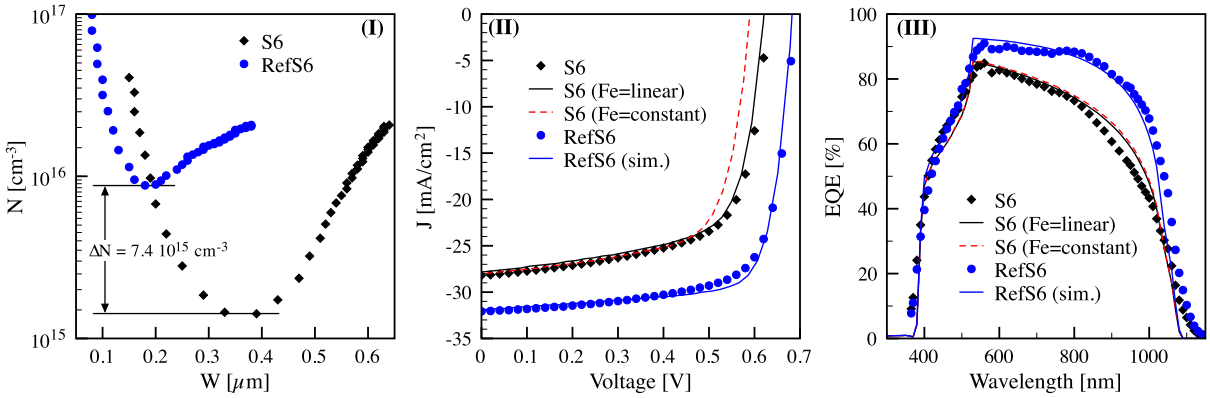

FIG. 9. Comparison of sample S6 and RefS6. The carrier density *N* (I) of S6, measured with CV, is ~3.5 times lower compared to RefS6. JV (II) and EQE (III) curves show measured (symbols) and SCAPS-simulated (lines) values, where both the linearly graded and constant Fe defect concentration are shown. Best match was achieved with a linear Fe impurity profile, whereas for a constant profile the calculated V_{oc} is too low.

dependence is expected for the SCR recombination. Furthermore, it has to be noticed that the loss in spectral response of S6 increases with the wavelength (see Fig. 9, III), which indicates recombination of generated electron-hole pairs in the bottom part of the CIGS layer (QNR) owing to the larger transmission length of photons at higher wavelengths (600 to 1000 nm). For RefS6, no significant loss in spectral response for this wavelength interval is visible. Therefore, the recombination in S6 can be attributed to the $Fe_{In,Ga}$ defects in the CIGS absorber.

V. CONCLUSIONS

In this work, two different process conditions for magnetron sputtered Mo back contact films were investigated on stainless steel foils. These conditions were used to grow several single- and multilayer back contact designs, which were used for CIGS solar cells deposited with a multistage process at low substrate temperature ($T_{max} = 475\,°C$).

Single layer back contact results show that the film density and residual stress strongly depend on both the film thickness and deposition conditions of the sputtering process, which is in accordance with literature. For multilayer designs, which represent a combination of two Mo layers deposited at different conditions, a relaxed stress state at a relatively high film density was achieved. Furthermore, the microstructure of the Mo bilayer shows a continuous interface of the columnar grains. Thus we conclude that the upper layer is affected by the grain structure of the first denser Mo layer, which explains the improvement in the overall density of the multilayer stack.

A strong correlation between the Mo back contact density and diffusion barrier performance against Fe was observed. Moreover, a clear dependence of the solar cell efficiency on the Fe concentration in the CIGS layer was found, where an increasing Fe amount leads to lower fill-factor, V_{oc} and J_{sc} values. The authors suggest that the loss in efficiency originates from deep acceptor defects, which are from Fe located at In/Ga site in the CIGS lattice. ToF-SIMS results show that the Fe impurity distribution in CIGS follows a linear concentration gradient, which decreases towards the CdS buffer layer. This linear trend of the Fe defect distribution in

RIGHTSLINK

CIGS was implemented in SCAPS device simulations, where the measured JV and EQE curves were successfully reproduced. The carrier concentration for the sample with high Fe impurity concentration in CIGS is significantly lower compared to its reference. This leads to the interpretation, that Fe is also present at Cu sites in the CIGS absorber and therefore reduces the acceptor concentration, owing to a lower density in Cu vacancies.

This report confirms that a multistage CIGS evaporation process at low substrate temperature reduces the diffusion barrier requirements, where a ~500 nm thick Mo bilayer acts sufficiently against Fe diffusion (sample S1). Additionally, this back contact design is free of residual film stress. With this configuration, high solar cell efficiencies above 15% were achieved with antireflection coating.

ACKNOWLEDGMENTS

This work was supported in part by the Swiss Federal Office for Energy (BFE), the Swiss Commission for Technology and Innovation (CTI, project no. 10245.1 PFNM-NM) and the European Union under project hipoCIGS (FP-7, contract no. 241384). In addition, the authors would like to thank D. Hosseini from Empa for performing the STEM measurements.

[1]P. Jackson, D. Hariskos, E. Lotter, S. Paetel, R. Wuerz, R. Menner, W. Wischmann, and M. Powalla, Prog. Photovoltaics **19**, 894 (2011).
[2]A. Chirilă, S. Buecheler, F. Pianezzi, P. Bloesch, C. Gretener, A. R. Uhl, C. Fella, L. Kranz, J. Perrenoud, S. Seyrling, R. Verma, S. Nishiwaki, Y. E. Romanyuk, G. Bilger, and A. N. Tiwari, Nature Mater. **10**, 857 (2011).
[3]F. Pianezzi, A. Chirilă, P. Blösch, S. Seyrling, S. Buecheler, L. Kranz, C. Fella, and A. N. Tiwari, Prog. Photovoltaics **20**, 253 (2012).
[4]R. Wuerz, A. Eicke, M. Frankenfeld, F. Kessler, M. Powalla, P. Rogin, and O. Yazdani-Assl, Thin Solid Films **517**, 2415 (2009).
[5]T. Satoh, Y. Hashimoto, S. Shimakawa, and T. Negami, Solid State Phenom. **93**, 127 (2003).
[6]K. Herz, A. Eicke, F. Kessler, R. Wächter, and M. Powalla, Thin Solid Films **431–432**, 392 (2003).
[7]M. S. Kim, J. H. Yun, K. H. Yoon, and B. T. Ahn, Solid State Phenom. **124–126**, 73 (2007).
[8]S. Niki, AIST Today **43**, 19 (2012).
[9]H. Park, S. C. Kim, H. C. Bae, T. Cheon, S.-H. Kim, and W. K. Kim, Mol. Cryst. Liq. Cryst. **551**(1), 147–153 (2011).
[10]P. Blösch, A. Chirilă, F. Pianezzi, S. Seyrling, P. Rossbach, S. Buecheler, S. Nishiwaki, and A. N. Tiwari, IEEE J. Photovoltaics **1**, 194 (2011).
[11]K. Otte, L. Makhova, A. Braun, and I. Konovalov, Thin Solid Films **511–512**, 613 (2006).
[12]A. P. Sutton and R. W. Balluffi, *Interfaces in Crystalline Materials* (Oxford University Press, 2007).
[13]I. Petrov, P. B. Barna, L. Hultman, and J. E. Greene, J. Vac. Sci. Technol. A **21**, 117 (2003).
[14]G. E. Murch and A. S. Nowick, *Diffusion in Crystalline Solids* (Academic, 1984), p. 482.
[15]D. Gupta, *Diffusion Processes in Advanced Technological Materials* (William Andrew, 2005), p. 532.
[16]P. Heitjans and J. Kärger, *Diffusion in Condensed Matter* (Springer Verlag, 2005), p. 965.
[17]J. C. Fisher, J. Appl. Phys. **22**, 74 (1951).
[18]O. Lundberg, J. Lu, A. Rockett, M. Edoff, and L. Stolt, J. Phys. Chem. Solids **64**, 1499 (2003).
[19]R. Schlesiger, C. Oberdorfer, R. Würz, G. Greiwe, P. Stender, M. Artmeier, P. Pelka, F. Spaleck, and G. Schmitz, Rev. Sci. Instrum. **81**, 043703 (2010).
[20]C. Tablero, J. Phys. Chem. A **116**, 1390 (2012).
[21]J. Haider, M. Rahman, B. Corcoran, and M. Hashmi, J. Mater. Process. Technol. **168**, 36 (2005).
[22]D. Rudmann, G. Bilger, M. Kaelin, F.-J. Haug, H. Zogg, and A. N. Tiwari, Thin Solid Films **431–432**, 37 (2003).
[23]D. Rudmann, D. Brémaud, H. Zogg, and A. N. Tiwari, J. Appl. Phys. **97**, 1 (2005).
[24]I. C. Noyan and J. B. Cohen, *Residual Stress—Measurement by Diffraction* (Springer, New York, 1987), p. 276.
[25]J. Lu, *Handbook of Measurement of Residual Stresses*, 1st ed. (Fairmont, Lilburn, 1996), p. 238.
[26]J. A. Thornton, J. Vac. Sci. Technol. **11**, 666 (1974).
[27]R. E. Cuthrell, D. M. Mattox, C. R. Peeples, P. L. Dreike, and K. P. Lamppa, J. Vac. Sci. Technol. A **6**, 2914, (1988).
[28]S. A. Pethe, E. Takahashi, A. Kaul, and N. G. Dhere, Sol. Energy Mater. Sol. Cells **100**, 1 (2012).
[29]J. H. Scofield, A. Duda, D. Albin, B. L. Ballard, and P. K. Predecki, Thin Solid Films **260**, 26 (1995).
[30]J. Ziegler, *SRIM—The Stopping and Range of Ions in Matter*, http://www.srim.org (2012).
[31]*CRC Handbook of Chemistry and Physics*, edited by D. R. Lide, 90th ed. (CRC, 2009), p. 2804.
[32]F. Klabunde, M. Lohmann, J. Blasing, and T. Drusedau, J. Appl. Phys. **80**, 6266 (1996).
[33]P. Blösch, D. Güttler, A. Chirilă, and A. N. Tiwari, Thin Solid Films **519**, 7453 (2011).
[34]T. Eisenbarth, R. Caballero, C. A. Kaufmann, A. Eicke, and T. Unold, Prog. Photovoltaics **20**, 568 (2012).
[35]S. Zhang, S. Wei, A. Zunger, and H. Katayama-Yoshida, Phys. Rev. B **57**, 9642 (1998).
[36]H. Neumann, E. Nowak, and G. Kuhn, Cryst. Res. Technol. **16**, 1369 (1981).
[37]G. S. Porras and S. M. Wasim, Phys. Status Solidi A **133**, 509 (1992).
[38]M. Burgelman, P. Nollet, and S. Degrave, Thin Solid Films **361–362**, 527 (2000).
[39]M. Gloeckler, A. L. Fahrenbruch, and J. R. Sites, in *Proceedings of the 3rd World Conference on Photovoltaic Energy Conversion* (2003), pp. 491–494.
[40]U. Rau and H. W. Schock, Appl. Phys. A **69**, 131 (1999).

RIGHTSLINK